



Nanodrug with dual-sensitivity to tumor microenvironment for immuno-sonodynamic anti-cancer therapy



Jinsheng Huang ^{a,1}, Zecong Xiao ^{b,1}, Yongcheng An ^c, Shisong Han ^c, Wei Wu ^d, Yong Wang ^{a,**}, Yu Guo ^{e,***}, Xintao Shuai ^{a,b,*}

^a College of Chemistry and Materials Science, Jinan University, Guangzhou, 510632, China

^b PCFM Lab of Ministry of Education, School of Materials Science and Engineering, Sun Yat-sen University, Guangzhou, 510275, China

^c Department of Minimally Invasive Interventional Radiology, and Laboratory of Interventional Radiology, the Second Affiliated Hospital of Guangzhou Medical University, Guangzhou, 510275, China

^d Department of Medical Oncology, the First Affiliated Hospital, School of Medicine, Zhejiang University, Hangzhou, 310003, China

^e Department of General Surgery, the First Affiliated Hospital of Sun Yat-Sen University, Guangzhou, 510275, China

ARTICLE INFO

Keywords:

Tumor-targeting immunotherapy
Melanoma
Combination therapy
Immune checkpoint blockade (ICB)
Sonodynamic therapy (SDT)

ABSTRACT

Although a combination with photodynamic therapy (PDT) is a potential means to improve the immune checkpoint blockade (ICB)-based anticancer immunotherapy, this strategy is subjected to the extremely poor light penetration in melanoma. Herein, we develop a lipid (LP)-based micellar nanocarrier encapsulating sonosensitizer chlorin e6 (Ce6) in the core, conjugating anti-PD-L1 antibody (aPD-L1) to the interlayer through MMP-2-cleavable peptide, and bearing a PEG coating sheddable at low pH value (≈ 6.5) of tumor microenvironment. The unique nanocarrier design allows a tumor-targeting delivery to activate the anti-tumor immunity and meanwhile to reduce immune-related adverse effects (irAEs). Moreover, a sonodynamic therapy (SDT) is triggerable by using ultrasonic insonation to produce tumor-killing reactive oxygen species (ROS), thereby bypassing the poor light penetration which restricts PDT in melanoma. A combination of SDT with aPD-L1 immunotherapy effectively promotes tumor infiltration and activation of cytotoxic T cells, which resulted in robust anti-cancer immunity and long-term immune memory to effectively suppress melanoma growth and postoperative recurrence. This strategy for tumor-targeting codelivery of immune checkpoint inhibitors and SDT agents could be readily extended to other tumor types for better immunotherapeutic outcome and reduced irAEs.

1. Introduction

Melanoma is one of the most aggressive malignancies with increasing incidence around the world [1]. Traditional chemotherapy and radiotherapy often fail in treating the advanced-stage inoperable melanoma [2], which makes it an imperative to develop other effective therapeutic means. In recent years, photodynamic therapy (PDT), with localized treatment nature favorable for achieving ideal therapeutic outcome and low side effects simultaneously, has attracted much attention in cancer treatment. It irradiates tumor sites with near-infrared (NIR) light to generate reactive oxygen species (ROS) such as singlet oxygen (${}^1\text{O}_2$), which can kill cancer cells effectively [3]. Unfortunately,

despite the advantage of the NIR light in penetrating tissue [4], the deposition of massive light-absorbing melanin in melanoma significantly reduces the penetration depth of NIR light, which makes the deeply situated cancer cells inaccessible to NIR light and consequently leads to limited anti-melanoma effect of PDT [5]. In such context, sonodynamic therapy (SDT) seems to be an ideal alternative to PDT in consideration that it employs a focal low intensity ultrasound without difficulty in penetrating any soft tissues to induce local production of the cancer cells-killing ROS [6,7]. It is well known that, unlike any light irradiation, ultrasound irradiation is not affected by melanin at all and can reach a penetration depth of tens of centimeters in soft tissues [8]. In addition, ultrasound irradiation can be focused on the tumor tissue more

* Corresponding author. College of Chemistry and Materials Science, Jinan University, Guangzhou, 510632, China.

** Corresponding author.

*** Corresponding author.

E-mail addresses: wangy488@jnu.edu.cn (Y. Wang), guoyu35@mail.sysu.edu.cn (Y. Guo), shuaixt@mail.sysu.edu.cn (X. Shuai).

¹ These authors contributed equally.

precisely than the light irradiation, thus reducing damage to healthy tissues. These features make SDT potentially a safe and feasible therapeutic means not only for various tumors located deep but also for the melanin-enriched melanoma which strongly restricts an application of PDT [9]. On the other hand, SDT was reported to induce acute inflammation which promotes lymphocytes infiltration in tumor, thus triggering an anti-tumor immunity [10]. However, SDT-triggered anticancer immunity was somewhat too transient and delicate to inhibit tumor growth and recurrence effectively. For highly effective melanoma treatment, SDT may need to synergize with other immunotherapeutic drugs to elicit robust anti-cancer immunity and long-term immune memory.

As a crucial self-protecting immune checkpoint molecule, programmed death-1 ligand (PD-L1, B7-H1) is utilized by cancer cells to provide defense against the host immune system [11]. Thus, immune checkpoint blockade using anti-PD-L1 antibody (aPD-L1) to prevent tumor immune escape is a promising strategy to combat cancer [12]. Moreover, the utilization of aPD-L1 in combination with other therapeutic means has proven highly effective in treating a variety of tumors [13]. For example, Chen et al. demonstrated that a combination of SDT with free aPD-L1 induced a robust anti-tumor response, which resulted in a synergistic effect to suppress the progression of 4T1 breast cancer and its lung metastasis [10]. However, PD-L1 is also expressed on normal tissues such as vascular endothelial cells, hepatocytes, and pancreatic islet cells, etc [14]. Thus, a large portion of the free aPD-L1 may bind to normal tissues after conventional intravenous administration, which not only leads to low intratumoral aPD-L1 concentration and insufficient antitumor immunity but also provokes non-specific immune amplification and on-target off-tumor immune-related adverse effects (irAEs) including pneumonitis, hepatitis, and nephritis with grade 3–4

adverse reaction [14,15]. Obviously, developing potent tumor-targeting aPD-L1 delivery strategies to simultaneously enhance the anticancer efficacy and reduce irAEs is of great importance at present [16].

In general, a tumor-targeting aPD-L1 delivery system needs to integrate several key characteristics including a safe carrier having potential to be approved by Food and Drug Administration (FDA), stealth property to avoid aPD-L1 binding with PD-L1 on normal tissues, and rapid aPD-L1 release once accumulated in tumor interstitium. On the other hand, the two different drugs employed in a combination therapy may possess very different pharmacokinetics, making it impossible to well control the drug ratio and distribution inside tumor. Consequently, the synergistic anticancer effect of two drugs could be greatly limited when the drugs are separately delivered, which underlines the importance of developing a potent nanocarrier to mediate tumor-targeting codelivery of two different types of drugs in a combination therapy. Indeed, recent studies have shown that nanocarriers-mediated co-delivery may unify the pharmacokinetics of two drugs and better control the intratumoral drug ratio and distribution to result in better anticancer outcome than the separate delivery [17,18]. Thus, a good synergistic effect of SDT and ICB-based immunotherapy in melanoma depends critically on a tumor-targeting co-delivery of the sonosensitiser and aPD-L1.

Herein, aiming to improve the immunotherapeutic efficacy and to reduce irAEs in melanoma treatment, we constructed a pH and MMP-2 dual-sensitive nanodrug incorporating aPD-L1 and sonosensitiser Ce6 based on the micellar assembly of FDA-approved lipids, i.e. PEG-CDM-aPD-L1/Ce6 abbreviated as P-aPD-L1/C (Fig. 1). The sonosensitiser Ce6 was loaded into the core of nanodrug through hydrophobic interaction, and the immune checkpoint antibody aPD-L1 was covalently conjugated to its interlayer via a MMP-2-cleavable peptide linker. Furthermore, PEG chains were conjugated through an acid-labile amide

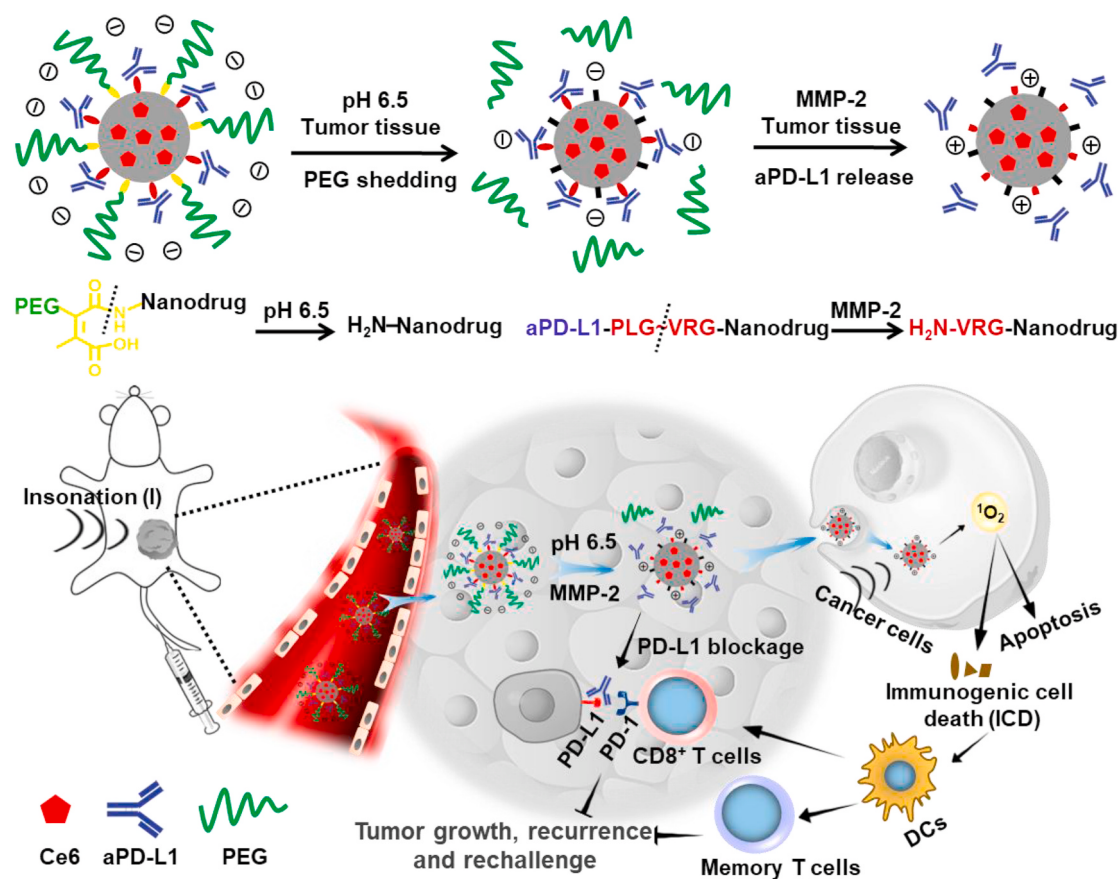


Fig. 1. Schematic illustration of the sensitivity and *in vivo* performance of the pH and MMP-2 dual-sensitive PEG-coated nanodrug PEG-CDM-aPD-L1/Ce6 abbreviated as P-aPD-L1/C for tumor-targeting immuno-sonodynamic combination therapy of cancer.

bond to form a sheddable PEG coating, which may endow the nanodrug with a stealth capability to avoid the off-target interaction between aPD-L1 and PD-L1 expressed on normal cells. After accumulation in tumor tissue, a shedding of PEG outer layer of nanodrug may be triggered by the tumor tissue acidity [19]. Then, the peptide linker for aPD-L1 may be cleaved by MMP-2 overexpressed in tumor tissue, resulting in the aPD-L1 release to reinvigorate T cell anti-cancer immunity. On the other hand, the Ce6-mediated SDT may be triggered by ultrasonic insonation to induce immunogenic cell death (ICD), which may promote the immune activation and tumor infiltration of T cells. Consequently, the SDT without the tissue-penetrating limitation in melanoma may synergize with the aPD-L1 treatment to elicit robust anti-cancer immunity and long-term immune memory. Provided that the therapeutic potency of this nanodrug can be verified, the strategy for tumor-targeting code-delivery of immune checkpoint inhibitors and SDT agents may be readily extended to the treatments of various tumors other than melanoma.

2. Materials and methods

2.1. Materials

1,2-distearoyl-sn-glycero-3-phosphocholine (DSPC), and 1,2-distearoyl-sn-glycero-3-phosphoethanolamine (DSPE), and fluorescein isothiocyanate (FITC)-conjugated DSPE (DSPE-FITC) were purchased from Advanced Vehicle Technology (China). Chlorin e6 (Ce6), DBCO-PEG₄-NHS ester, and sulfo-cyanine 3 NHS ester (Cy3-NHS) were purchased from Sigma-Aldrich. The MMP-2 sensitive peptide GGPLGVRRGGK(N₃)-NH₂ was synthesized using solid phase peptide synthesis (SPSS) according to our recent report [18]. The MnO nanoparticle was prepared using a solvothermal method [20]. The IFN- γ was purchased from PeproTech. Other reagents and antibodies (Table S1) were used as received without further purification. Matrix metalloproteinase-2 (MMP-2) was purchased from R&D Systems (Minneapolis). The detailedly synthesized procedures of DSPE-DBCO, Mal-GGPLGVRRGG-K(N₃)-NH₂, N₃-peptide-conjugated antibody, and mPEG-CDM were shown in Scheme S1-S4.

2.2. Preparation and of pH and MMP-2 dual-sensitive nanodrug

First, the Ce6-loaded lipid-based nanoparticle was prepared as follows (Fig. S3). A 40: 1: 5 molar ratio of DSPC: DSPE-DBCO: DSPE (a total of 30 mg) and 2.2 mg of Ce6 were dissolved in a mixture of 8 mL of CH₂Cl₂ and 2 mL of MeOH. The resulted solution was added into 9 mL of deionized water under sonication. After CH₂Cl₂ was removed by rotary evaporation, the solution was dialyzed against water (MWCO: 14 k), and concentrated by ultrafiltration. Second, N₃-peptide-conjugated antibody or N₃-peptide-conjugated Cy3-labeled antibody was added and vortexed for 8 h. Third, mPEG-CDM was added and vortexed for 2 h at room temperature. The free antibody and PEG were removed by dialysis, thus obtaining PEG-coated and aPD-L1-modified nanoparticle (P-aPD-L1/C). The PEG-coated and isotype control antibody (Iso)-modified nanoparticle (P-Iso/C) was also prepared using the above method. Nanoparticle without PEG coating (e.g., aPD-L1/C) was prepared as control. After 1.0 wt% Triton X-100 was added into the nanoparticle solution, the Ce6 and antibody loading contents were quantified by fluorescence spectrophotometer (Shimadzu RF5301, Japan). The excitation wavelengths of Ce6 and Cy3 were 400 and 530 nm, respectively. The emission wavelengths of Ce6 and Cy3 were 670 and 570 nm, respectively.

2.3. Characterization

¹H NMR spectra were recorded on a Bruker 400 MHz spectrometer at 25 °C. The molecular weight of compound was determined by ion trap mass spectrometer (Thermo LTQ XL, USA). Particle size and zeta potential were measured by dynamic light scattering (DLS) at 25 °C (Malvern NANO ZS, UK). Samples were incubated with or without MMP-

2 in PBS (pH 7.4 or 6.5) before DLS measurements. The sample on carbon film-coated copper grid was stained with uranyl acetate (0.5 wt %), and observed under transmission electron microscopy (Hitachi H-7650, Japan). The release amount of PEG was analyzed on a gel permeation chromatography (GPC) system using refractive index detector at 40 °C. The LiBr (1 g/L)-containing DMF was used as the mobile phase with a 1.0 mL/min flow rate [21]. The mPEG-OH with a molecular weight of 5 kDa (Sigma-Aldrich) was used for standard curve.

2.4. Tumor acidity-triggered PEG shedding and MMP-2-triggered antibody release *in vitro*

The MMP-2-triggered antibody release was qualitatively assessed by fluorescence resonance energy transfer (FRET) between Cy3-labeled aPD-L1 and FITC-labeled lipid in one nanodrug (P-aPD-L1-Cy3/FITC). The solution containing P-aPD-L1-Cy3/FITC (Cy3, 0.1 µg/mL; FITC, 0.3 µg/mL) was incubated at different pH (*i.e.*, 7.4 or 6.5) and MMP-2 concentrations (*i.e.*, 0.5 or 10 nM). The emission spectra of Cy3 and FITC were recorded under a maximum excitation wavelength of FITC at 480 nm.

To investigate the quantitative PEG and aPD-L1 release, the P-aPD-L1-Cy3 nanodrug in 3 mL of PBS (pH 7.0 or 6.5) was prepared with different MMP-2 concentrations. In another group, 2.5 mL of serum was added into 0.5 mL of nanodrug solution without MMP-2. The solution was transferred into a dialysis bag (MWCO: 500 kDa) which was then immersed in a centrifuge tube containing 8 mL of PBS and shaken at 37 °C. 4 mL of the solution outside the dialysis bag was replaced with 4 mL of fresh PBS for further analysis at certain time intervals. The cumulative release of PEG and antibody were detected by GPC analysis and fluorescence spectrophotometry, respectively.

2.5. Cell culture

A mouse melanoma cell line of B16-F10 was purchased from Cold Spring Biotech Corp (China) and cultured in Dulbecco's modified Eagle's medium (DMEM, Gibco) containing 10% fetal bovine serum (FBS, Gibco) and 1% penicillin/streptomycin under a humidified atmosphere of 5% CO₂ at 37 °C.

2.6. Shielding and restoration of binding functionality of aPD-L1 *in vitro*

Hepatocytes were isolated from C57BL/6 mouse according to our recent report [21] and stimulated with IFN- γ (500 U/mL) for 6 h to enhance its PD-L1 expression [22]. Then, the PD-L1-overexpressed B16-F10 cells and hepatocytes were incubated with P-aPD-L1-Cy3 nanodrug at different pH and MMP-2 concentration. Meanwhile, free aPD-L1 and Iso were used as a positive control and a negative control, respectively. Finally, the aPD-L1-Cy3-positive cells were then measured on a confocal laser scanning microscope (CLSM, Carl Zeiss LSM 710) and flow cytometry (Gallios).

2.7. Cellular uptake

B16-F10 cells were cultured with P-aPD-L1/C at different incubated condition. Then, the cells were washed with PBS, fixed by paraformaldehyde, stained with 4',6-diamidino-2-phenylindole (DAPI), and imaged on a CLSM. In addition, the cellular uptake of P-aPD-L1/C was quantitatively analyzed by flow cytometry. Excitations: 488 nm for Ce6 and 405 nm for DAPI; emissions: 670 nm for Ce6 and 455 nm for DAPI.

2.8. Detection of ROS generation

The ROS generation of P-aPD-L1/C triggered by ultrasonic insonation was detected by using singlet oxygen sensor green (SOSG, ThermoFisher) probe whose fluorescence would increase upon reaction with insonation-induced ¹O₂ mediated by Ce6 [23]. Nanodrug solution

containing 0.5 μM SOSG at a Ce6 concentration of 1 μM was exposed to insonation (2.0 MHz, 2.0 W/cm², 20% duty cycle) for different time. The fluorescence of SOSG was determined on a fluorescence spectrophotometer using an excitation of 480 nm. In addition, ROS levels inside cells and tumor tissue after ultrasonic insonation were evaluated by using 2',7'-dichlorofluorescein diacetate (DCFH) [24].

2.9. Cell viability and apoptosis

B16–F10 cells were treated with nanodrugs at pH 7.4 or pH 6.5 + 10 nM MMP-2 for 6 h, insonated (2 MHz, 2.0 W/cm², 20% duty cycle) for 5 min, and further incubated for various times. The cell viabilities were measured by MTT assay. In addition, the cell viabilities were evaluated by using live/dead cell imaging kit (ThermoFisher). Moreover, the ROS-induced cell apoptosis was detected by using 7-AAD/Annexin V-FITC dual-staining assay and measured on a flow cytometer.

2.10. Animal model

C57BL/6 mice were purchased from the Guangdong Medical Laboratory Animal Centre. All experiments on animal were under the guideline of the Institutional Animal Care and Use Committee of the Sun Yat-sen University. 1×10^6 B16–F10 cells suspended in 100 μL of PBS were subcutaneously implanted into the 4- to 6-week old mice at the right hind leg to establish the animal tumor model.

2.11. Biodistribution and pharmacokinetics of nanodrug *in vivo*

When the tumor volume grew to $\sim 60 \text{ mm}^3$, the mice ($n = 3$) was intravenously injected with P-aPD-L1/MnO and aPD-L1/MnO nanodrug (10 mg Mn per kg body weight) via the tail vein, respectively. At pre-determined time points, the blood samples were collected for pharmacokinetics investigation. The Mn concentration in blood was measured by using inductively coupled plasma optical emission spectrometry (ICP-OES). In addition, the major organs and tumor were excised at 24 h post intravenous injection, weighed, and digested by concentrated nitric acid. The Mn concentration in solution was measured by using ICP-OES after dilution with water and filtration.

2.12. Magnetic resonance imaging (MRI) *in vivo*

The tumor-bearing mice ($n = 3$) were intravenously injected with P-aPD-L1/MnO and aPD-L1/MnO nanodrug, respectively. The T1-weighted images were acquired on a 3.0-T MRI apparatus (Ingenia, Philips Medical Systems, Netherlands) with an animal coil. The mean T1 signal intensities of three transverse sections of tumor were calculated, and the signal intensities of muscle in the same section was used as the internal reference.

2.13. Synergistic anti-cancer effect *in vivo*

The tumor-bearing mice were randomly divided into five groups and received the treatment of PBS, P-aPD-L1/C, P-Iso/C + insonation, aPD-L1/C + insonation, and P-aPD-L1/C + insonation, respectively. The doses of aPD-L1 and Ce6 were both 5 mg/kg body weight per injection at an interval of 2 d for 5 times. The tumors were exposed to ultrasonic insonation (2.0 MHz, 2.0 W/cm², 20% duty cycle, 10 min) at 24 h post-administration of nanodrug. The mice survival rate and body weight were recorded and plotted against time. In addition, the tumor volumes were calculated by using the following formula: Volume = $0.5 \times L \times W^2$, in which the L and W indicate the length and width of the tumor.

To study the immune memory effect, the primary tumor-bearing mice were received various treatments. After the primary tumors were resected, the mice were rechallenged a secondary B16–F10 tumor at the left hind leg. The recurrence of resected primary tumor and growth of secondary tumor were recorded at certain time intervals.

2.14. Analysis of immune cells by flow cytometry

The tumors were excised from mice receiving various treatments, and homogenized to single cell suspensions in PBS. In addition, the blood samples were collected for immune memory study. The live T lymphocytes were purified by using the Ficoll-Hypaque solution (MP Biomedicals, USA), stained with antibodies (e.g., anti-CD3, anti-CD4, anti-CD8, anti-IFN- γ , anti-CD62L, and anti-CD44), and fluorophore-labeled secondary antibody if required. The subpopulations of T cells were finally analyzed on a flow cytometer.

2.15. Biochemistry index and histology analysis

On day 15 after the first treatment, serums of mice were collected to test the biomedical indexes on an autobiochemical analyzer (Rayto Chemray 240, China). Tumors and major organs were excised, fixed, deparaffinized, and sliced for $\sim 5 \mu\text{m}$ thickness. The tissue sections, at least three per animal, were subjected to H&E and immunohistochemical staining.

2.16. Statistical analysis

Data are presented as the mean \pm standard deviation (SD). Statistical analyses were performed using ANOVA with a Tukey's test. $P < 0.05$ was considered to be statistically significant.

3. Results and discussion

3.1. Preparation and characterization of nanodrug

As shown in Scheme S1, the dibenzocyclooctyne (DBCO)-capped lipid (DSPE-DBCO) was synthesized via a coupling reaction between 1,2-distearoyl-sn-glycero-3-phosphorylethanolamine (DSPE) and NHS-activated DBCO. The successful synthesis of DSPE-DBCO was verified by ¹H NMR and mass spectrometric analyses (Fig. S1-S2). Then, the pH and MMP-2 dual-sensitive nanodrug being decorated with a sheddable PEG coating and carrying aPD-L1 and Ce6, which was denoted as P-aPD-L1/C, was prepared via multi-step reactions (Scheme S2-S4 and Fig. S3). Firstly, 1,2-dioctadecanoyl-sn-glycero-3-phosphocholine (DSPC), DSPE-DBCO, and DSPE with a molar ratio of 40, 1 and 5 were used to fabricate a core-shell micelle encapsulating the sonodynamic agent Ce6 in its core using a nanoprecipitation method [25]. Then, the anti-PD-L1 antibody (aPD-L1) with a tail of MMP-2-sensitive peptide GGPLGVRRGG-N₃ was anchored to the Ce6-loaded nanoparticle through the copper (I)-free click reaction between the DBCO groups of nanoparticle and azide groups (-N₃) of aPD-L1-peptide (Scheme S2-S3 and Fig. S3) [26]. Finally, the carboxy-dimethylmaleic anhydride (CDM)-terminated mPEG (Scheme S4 and Fig. S3) was covalently conjugated to the nanoparticle through forming an amide linkage sensitive to tumor microenvironment acidity (≈ 6.5) [19], which hopefully may prevent aPD-L1 from interaction with normal cells. Based on the block copolymer of polyethylene glycol (PEG) and polyaspartic acid (diisopropyl ethylenediamine-co-benzylamine), we recently developed a dual-sensitive micelle which encapsulated paclitaxel in its core and conjugated anti-PD-1 antibody (aPD-1) to its interlayer via a Cu (I)-catalyzed click reaction. The codelivery of paclitaxel and aPD-1 resulted in a synergistic chemoimmunotherapy of melanoma in mice [27]. However, we were also aware that the complicated polymer structure and hard removal of Cu (I) may impede its clinical translation. In comparison, this study used the FDA-approved lipid materials as nanocarriers and a Cu (I)-free click reaction for antibody conjugation, which may greatly improve the clinical translation potential of the delivery system.

The loading contents of Ce6 and antibody were measured to be 5.6% and 3.5%, respectively. The nanodrugs free of PEG and Ce6, i.e. aPD-L1/C and P-aPD-L1, respectively (Table S2), were prepared by the same

method. Phospholipids can be made into multiple types of assemblies such as micelle, liposomes, and hexagonal phase by adjusting the component of lipids and assembly methods [28]. In this study, Ce6-loaded lipid-based particulate micelles were prepared at a 40: 1: 5 molar ratio of DSPC: DSPE-DBCO: DSPE (a total of 30 mg) and 2.2 mg of Ce6 under ultrasonic dispersion, as revealed by TEM (Fig. 2a). In addition, TEM observation revealed that the dual-sensitive nanodrug P-aPD-L1/C was spherical, and had a mean particle diameter of 52.9 ± 5.8 nm and uniform size distribution. The aPD-L1 antibody was clearly observed as black dots on the surface of nanodrug [29]. On average, each nanodrug particle was decorated with 10.1 ± 2.9 molecules of aPD-L1 antibody (Fig. 2a). The positive or negative staining of protein for electron microscopy is sample- and staining method-dependent [29, 30]. The abundant carboxylic groups (-COOH) of aPD-L1 antibody easily absorb uranyl ion (UO_2^{2+}) when the nanodrugs were stained with uranyl oxalate aqueous solution. The UO_2^{2+} -absorbed aPD-L1 antibodies were imaged as the black dots under TEM measurement because of its high electron density and high electron scattering capability relative to the surrounding stain. Furthermore, according to the dynamic light scattering (DLS) measurements, P-aPD-L1/C possessed a hydrodynamic diameter of 85.2 ± 4.0 nm, a narrow particle distribution index (PDI = 0.13) and a zeta potential of -23.1 ± 1.0 mV (Table S3). The particle size measured by TEM was smaller than that measured by DLS, most likely because the PEG outer layer with low electron density was hardly observable under TEM [18].

3.2. Tumor acidity-triggered PEG shedding and MMP-2-triggered antibody release

Most solid tumors were in a weakly acidic microenvironment (pH 6.5–6.8) with MMP-2 enzyme overexpression despite their heterogeneity [26,31]. The pH-sensitive shedding of PEG coating from nanodrug without Ce6 encapsulation (P-aPD-L1) was studied at pH 7.4 and pH 6.5, which are known for bloodstream and tumor tissue [31], respectively. Measurements with the gel permeation chromatography (GPC) showed

that very few PEG was released from P-aPD-L1 at pH 7.4 (Fig. 2b). In comparison, the PEG peak in the GPC eluogram became much more prominent when P-aPD-L1 was incubated at pH 6.5, indicating an efficient breakage of the pH-sensitive amide bonds to release PEG chains from nanoparticles. As shown in Fig. 2c, quantitative analysis further revealed that 77.5% of PEG was released in 6 h when incubating the nanodrug in a pH 6.5 solution. However, only 16.7% of PEG was released in 24 h when incubating the nanodrug in a pH 7.4 solution.

The nanocarrier and aPD-L1 were labeled with fluorescein isothiocyanate (FITC) and Cy3, respectively, which allowed the investigation of the MMP-2-triggered aPD-L1 release *in vitro* using a fluorescence resonance energy transfer (FRET) assay. Because the two fluorophores FITC (as a donor) and Cy3 (as an acceptor) are of intermolecular proximity at angstrom distances (10–100 Å) inside one nanodrug, a FRET would happen between them. However, release of the Cy3-labeled aPD-L1 from the FITC-labeled nanocarrier would turn off the FRET because of the too large distance between the two fluorophores. Both FITC and Cy3 displayed clear fluorescence emission peaks when the nanodrug (P-aPD-L1-Cy3/FITC) was irradiated by a 480 nm laser known for the maximum FITC excitation in the solution of pH 7.4 and 0.5 nM MMP-2 mimicking the microenvironment of normal tissue and bloodstream [18,26], which strongly indicated a FRET between them (Fig. 2d). Then, we varied the incubation time of nanodrug in the above solution to see whether the Cy3 and FITC fluorescence emission intensities would change at the same excitation and detection conditions. As shown in Fig. 2d, the incubation time of nanodrug showed almost negligible effect on the emission intensities of both fluorescent agents over 24 h, demonstrating that the Cy3-labeled antibody was hardly released from nanodrug at pH 7.4 + 0.5 nM MMP-2 (Fig. 2d). By contrast, when the nanodrug was incubated at pH 6.5 + 10 nM MMP-2 mimicking the tumor microenvironment condition, a change of incubation time of nanodrug from 0 h to 24 h exhibited a remarkable effect on the emission intensities of the two fluorescent agents. In other words, the prolonged nanodrug incubation time led to a marked decrease in the Cy3 fluorescence emission while an obvious increase in the FITC fluorescence emission (Fig. 2e), strongly

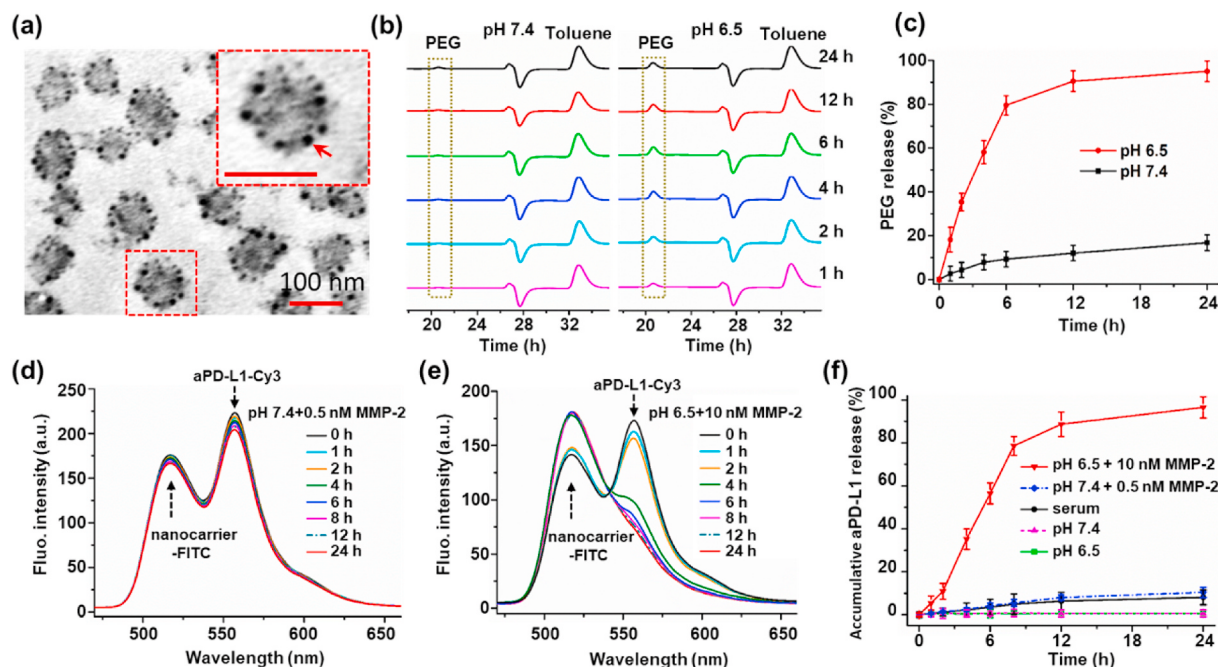


Fig. 2. Characterization and stimuli release of PEG and aPD-L1. (a) The morphology of P-aPD-L1/C observed under TEM. A nanodrug in red dotted box was enlarged for a clearer view. The red arrows indicated aPD-L1. Scale bars represent 100 nm. (b) GPC curves of the released PEG at pH 7.4 and 6.5 using toluene as an internal reference. (c) Cumulative release of PEG at pH 7.4 and 6.5 measured by GPC. (d–e) FRET between FITC-labeled nanocarrier and Cy3-labeled aPD-L1 in nanodrug (P-aPD-L1-Cy3/FITC) solution of (d) pH 7.4 + 0.5 nM MMP-2 or (e) pH 6.5 + 10 nM MMP-2. (f) Cumulative release of aPD-L1 from nanodrugs under different incubated condition *in vitro*. (For interpretation of the references to colour in this figure legend, the reader is referred to the Web version of this article.)

indicating the release of antibody which significantly weakened the FRET between FITC and Cy3 in this condition. Notably, the Cy3 fluorescence was hardly recorded when the nanodrug incubation exceeded 8 h in solution of pH 6.5 + 10 nM MMP-2, implying that almost all Cy3-aPD-L1 was released from nanodrug to completely terminate the FRET from FITC to Cy3. Quantitative measurements of the aPD-L1 release contents obtained consistent results (Fig. 2f). The aPD-L1 release was not detectable at both pH 7.4 and 6.5 in the absence of MMP-2. In contrast, a rapid aPD-L1 release was observed in the solution of 10 nM MMP-2 + pH 6.5. These results elucidated that an aPD-L1 release from nanodrug could be effectively triggered in tumor tissue featuring pH 6.5 and 10 nM MMP-2.

Although the tumor-targeting codelivery of immune checkpoint inhibitors and SDT agents could be achieved as well through a pH responsive release of both PEG and antibody, it is difficult to prepare such nanodrug. The bifunctional pH-sensitive CDM and other moieties were hard to conjugate the aPD-L1 antibody because the conjugation reaction must be carried out in anhydrous organic solvent (Scheme S4) that would lead to the inactivation of aPD-L1 antibody. Therefore, a water-soluble and bifunctional MMP-2-sensitive linker was adopted to conjugate aPD-L1 antibody (Scheme S3 and Fig. S3), and the pH-sensitive CDM was used to conjugate PEG (Scheme S4 and Fig. S3).

3.3. Shielding and restoration of aPD-L1 binding evaluated in vitro

To reduce immune-related adverse effects (irAEs) due to the off-target PD-L1 binding of aPD-L1 in normal tissues and in blood, the nanodrug was designed to hide the antibody during transportation but expose it after having accumulated in tumor site. The PD-L1-positive B16-F10 cancer cells and normal primary mouse hepatocytes were incubated with the pH and MMP-2 dual-sensitive nanodrug (P-aPD-L1-Cy3) in different conditions and then analyzed with confocal laser scanning microscopy (CLSM) to verify the cancer cell-specific binding potential, using the Cy3-labeled free aPD-L1 and Cy3-labeled isotype antibody (Iso) as the positive and negative controls, respectively [22]. As shown in Fig. S4a, the Cy3 fluorescence was hardly observed in both B16-F10 cells and hepatocytes incubated with P-aPD-L1-Cy3 at pH 7.4 no matter 0.5 nM MMP-2 was present or not. In contrast, both B16-F10 cells and normal hepatocytes incubated with P-aPD-L1-Cy3 at pH 6.5 showed much stronger Cy3 fluorescence, and cells incubated with P-aPD-L1-Cy3 at pH 6.5 + 10 nM MMP-2 displayed the strongest Cy3 fluorescence even comparable to that in cells incubated with free aPD-L1-Cy3. Quantitative analysis with flow cytometry achieved consistent results (Fig. S4b). The aPD-L1 binding efficiency of B16-F10 cells was less than 10% at pH 7.4 ± 0.5 nM MMP-2, whereas it was increased to 60% at pH 6.5. Notably, the aPD-L1 binding efficiency was above 95% in B16-F10 cells incubated with the dual-sensitive nanodrug at pH 6.5 + 10 nM MMP-2 or with free antibody.

These data are in line with the data of tumor acidity-triggered PEG shedding and MMP-2-triggered antibody release as introduced in the previous section. Obviously, the binding of aPD-L1 to PD-L1-positive cells in blood and normal tissues could be blocked because of the stable PEG shielding layer at pH 7.4. However, after the nanodrug accumulated in the tumor tissue, the acidic and MMP-2-enriched microenvironment may trigger the shedding of PEG coating and aPD-L1 release to allow a highly effective aPD-L1 binding to tumor cells. In the absence of 10 nM MMP-2, although the PEG shedding was triggered at pH 6.5 to expose the unreleased aPD-L1, the cancer cell binding efficiency of antibody was affected by the nanodrug to some extent.

Then, we further studied whether the aPD-L1 antibody was internalized prior to release from nanodrugs when the P-aPD-L1-Cy3 was incubated with PD-L1-positive B16-F10 cells under the tumor microenvironment-mimicking conditions. As shown in Fig. S5, most of aPD-L1-Cy3 bound to the membrane of PD-L1-positive B16-F10 cells and few aPD-L1-Cy3 was internalized into the cell for incubation time of both 4 h and 8 h. It is reasonable that the PEG coating and negative

charge of nanoparticles blocked its cellular internalization prior to PEG and aPD-L1 release [19], and the released aPD-L1 would bind to PD-L1 on the membrane of B16-F10 cells.

3.4. Cell uptake of sonosensitizer Ce6 and SDT assessments in vitro

As observed under CLSM, cells incubated with the pH and MMP-2 dual-sensitive nanodrug (P-aPD-L1/C) at pH 7.4 showed negligible Ce6 fluorescence (Fig. 3a). It once again demonstrated the stable PEG coating and negative charge of nanodrug at pH 7.4 effectively blocked its cell uptake [19]. In contrast, P-aPD-L1/C was efficiently internalized into the cancer cells at pH 6.5 + 10 nM MMP-2, and flow cytometry analysis verified that almost all B16-F10 cells were Ce6 fluorescence positive after incubation in the same conditions. Moreover, only 14.6% cells became Ce6 fluorescence positive after incubation at pH 7.4 without MMP-2 (Fig. 3b). Based on these results, removal of the PEG coating at pH 6.5 and cleavage of the MMP-2-sensitive peptide linking aPD-L1 would occur in tumor tissue, which caused the aPD-L1 release and a negative-to-positive transition of surface charge to promote the cell uptake of Ce6-loaded nanodrug.

The ROS generation of Ce6-loaded nanodrug under ultrasonic insonation (I) was measured with the singlet oxygen sensor green (SOSG) probe. The ROS produced by Ce6 under insonation in the nanodrug solution can react with SOSG to increase its fluorescence intensity, thus indicating the ROS level [23]. As shown in Fig. 3c, the ROS production was increased through prolonging the insonation time. The ROS-induced cytotoxicity of nanodrug was evaluated in B16-F10 melanoma cells. The B16-F10 cells still showed a high viability above 96% even after incubation with 1.5 mg/mL Ce6-free nanoparticle, indicating a good biocompatibility of the carrier itself (Fig. S6a). In addition, cells incubated under insonation without nanodrug showed no obvious decrease in cell viabilities in comparison with the cells incubated with PBS (control), and the same results were also obtained for cells incubated with P-aPD-L1/C at pH 7.4 or at pH 6.5 + 10 nM MMP-2 in the absence of insonation (Fig. S6b). These results suggested that neither the low intensity insonation without nanodrug nor the nanodrug (P-aPD-L1/C) without insonation was able to exert a cytotoxic effect. By contrast, obvious toxic effects were observed at all studied Ce6 concentrations if the cells were incubated with P-aPD-L1/C at pH 6.5 + 10 nM MMP-2 under insonation (Fig. 3d). Furthermore, when insonation was applied, cells incubated with P-aPD-L1/C showed much lower viability at pH 6.5 + 10 nM MMP-2 than at pH 7.4 without MMP-2. This result was in line with the aforementioned cell uptake data. At pH 6.5 + 10 nM MMP-2, the PEG coating and aPD-L1 were detached to facilitate the cell uptake of Ce6-loaded nanodrug. Moreover, a ‘negative-to-positive’ surface charge switching also occurred to further promote the Ce6 delivery into cancer cells because the cleavage of PEG and aPD-L1 linkers would result in the release of negatively charged aPD-L1 and production of amino groups on the nanodrug surface (Figs. 1, 3a and 3b, and Table S3) [19,27].

A ROS indicator, dichlorofluorescin diacetate (DCFH), was used to assess the sonoactivity of P-aPD-L1/C inside cells. According to CLSM observation (Fig. 3f), insonation induced the highest green fluorescence intensity in cells receiving P-aPD-L1/C at pH 6.5 + 10 nM MMP-2, suggesting a highly efficient ROS generation from Ce6 under insonation. The live and dead cell staining assay was performed to further investigate the cancer cell killing effect of the generated ROS. As shown in Fig. 3g, cells treated with PBS or P-aPD-L1/C under insonation showed strong green fluorescence at pH 7.4. In contrast, cells treated with P-aPD-L1/C under insonation showed very weak green fluorescence at pH 6.5 + 10 nM MMP-2, apparently owing to the ROS-induced cell death. Consistent results were obtained in quantitative analysis of cell apoptosis using flow cytometry (Fig. 3h). In other words, cells incubated with P-aPD-L1/C at pH 6.5 + 10 nM MMP-2 under insonation showed the highest apoptotic level reaching 61.5%, which demonstrated the high efficiency of SDT in inducing cell apoptosis in this

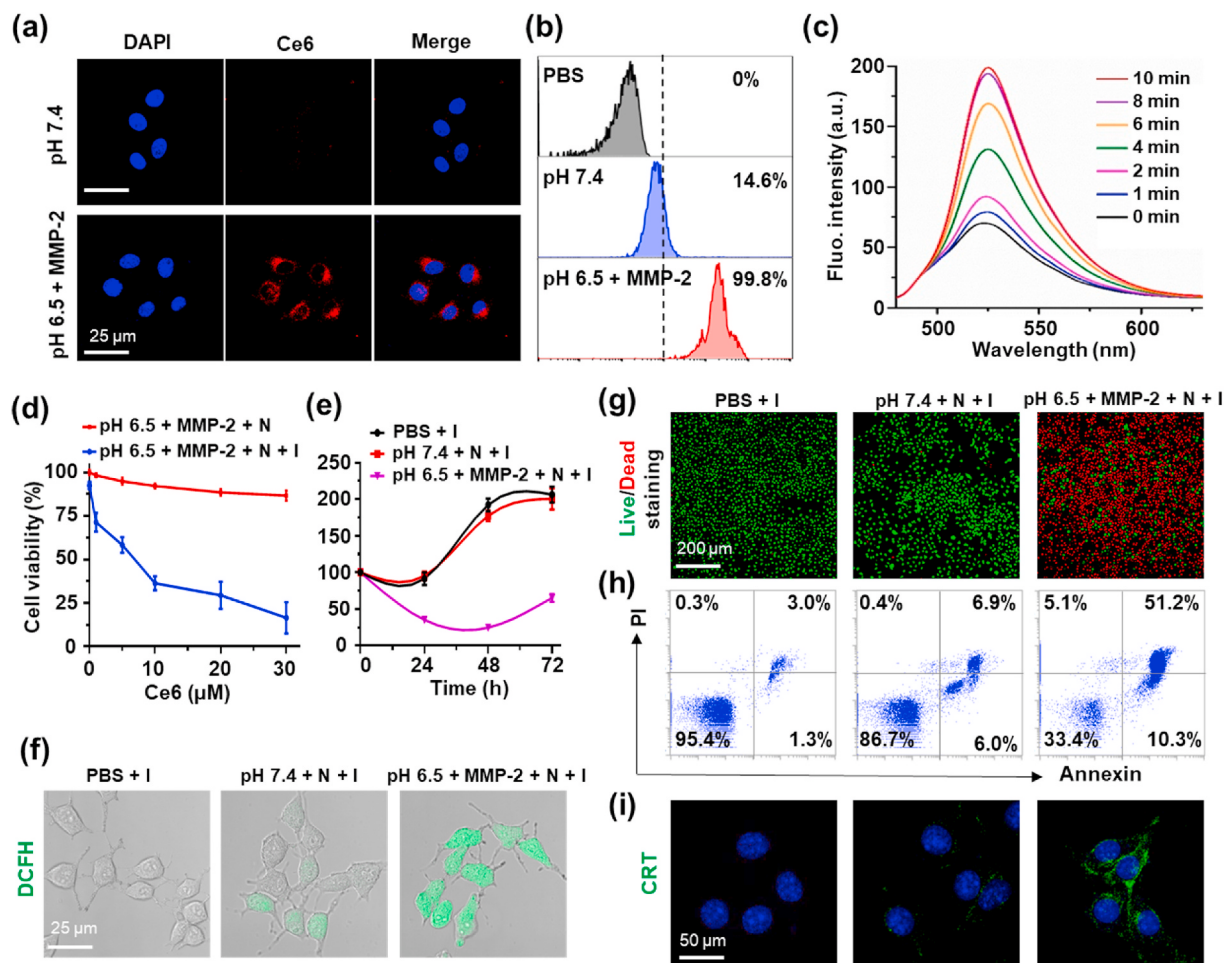


Fig. 3. Cellular uptake and SDT-mediated anti-cancer effect *in vitro*. (a–b) Cellular uptake of nanodrug measured by (a) CLSM and (b) flow cytometry. P-aPD-L1/C nanodrugs, which had been pretreated with pH 6.5 + 10 nM MMP-2 for 6 h, were added into the culture medium and incubated with cells for another 4 h. (c) Ultrasonic insonation (I)-triggered ROS production measured by the fluorescence probe of SOSG ($\lambda_{\text{ex}} = 488 \text{ nm}$). 1 μM Ce6 of P-aPD-L1/C was exposed to insonation (2.0 MHz, 2.0 W/cm², 20% duty cycle). (d) Viabilities of B16-F10 cancer cells after incubation with P-aPD-L1/C at pH 6.5 and MMP-2 with or without insonation for 24 h. (e) Insonation-triggered cytotoxic effect of P-aPD-L1/C on B16-F10 cancer cells after incubation with P-aPD-L1/C at different conditions. (f) Analyses of intracellular ROS level using DCFH as a ROS probe, (g) live and dead cell staining, (h) apoptosis analyses, and (i) immunofluorescence staining of CRT exposure. B16-F10 cells in Fig. f–i were incubated with P-aPD-L1/C for 6 h, treated with insonation (2 MHz, 2.0 W/cm², 20% duty cycle, 5 min), and incubated for another 24 h. PBS + insonation (I) was used as control group, and Ce6 concentration was 5.0 μM for (e–i). The MMP-2 concentration was 10 nM for (a–i) if added. N in the group label meant the nanodrugs of P-aPD-L1/C were added for (d–i). Data are shown as mean \pm SD, $n = 3$.

condition.

Admittedly, calreticulin (CRT) is a distinct biomarker of immunogenic cell death (ICD) which is a ‘eat me’ signal on the cell surface to mediate the engulfment of dying cancer cells and cancer-cell debris by immature dendritic cells (DCs) and to induce the succeeding anti-tumor immune response [32]. Thus, CRT exposed on the SDT-induced immunogenic phenotypes of B16-F10 cancer cells was tested using immunofluorescence assay. As shown in Fig. 3i, cells treated with PBS or P-aPD-L1/C under insonation showed negligible green fluorescence at pH 7.4. By contrast, cells treated with P-aPD-L1/C under insonation exhibited much stronger green fluorescence at pH 6.5 + 10 nM MMP-2, which clearly indicated an efficient ICD induced by SDT.

3.5. Biodistribution of P-aPD-L1/C *in vivo*

The melanin abundant in melanoma may absorb visible and near infrared lights to impede the Ce6 fluorescence imaging. To address this challenge, MnO known as tumor microenvironment-triggerable a T1 magnetic resonance imaging (MRI) agent was encapsulated in the hydrophobic cores of two micellar nanodrugs P-aPD-L1/MnO and aPD-L1/MnO [20]. After injecting nanodrug into the C57BL/6J mice via tail vein,

the pharmacokinetic profile of nanodrug was evaluated *via* measuring the content of Mn element in bloodstream with inductively coupled plasma optical emission spectrometry (ICP-OES) [20,33]. The elimination half-life was used as the circulation half-life ($t_{1/2}$). It was calculated as the time for half of the initial concentration of Mn element in blood after tail vein injection of MnO-encapsulated nanoparticles. The initial concentration of time point was set as 5 min after intravenous administration of nanoparticle in this study.

As shown in Fig. 4a, there was no significant difference ($P = 0.2935$) between Mn concentration of initialization and that of 1 h (50.02 ± 5.22 vs $44.90 \pm 4.02 \mu\text{g/mL}$) after tail vein injection of P-aPD-L1/MnO nanodrug using one-way ANOVA analysis. However, there was a highly significant difference ($P < 0.0001$) between Mn concentration of initialization and that of 1 h (48.18 ± 3.29 vs $33.35 \pm 3.71 \mu\text{g/mL}$) after tail vein injection of aPD-L1/MnO nanodrug using the same analytical method. Moreover, the blood circulation half-life ($t_{1/2}$) of the PEG-sheddable P-aPD-L1/MnO reached 13.5 h, which is much longer than that of aPD-L1/MnO (3.1 h). The quick clearance of aPD-L1/MnO from blood was most likely due to the binding of aPD-L1 to PD-L1-positive normal tissues, which was an undesirable on-target but off-tumor cell effect.

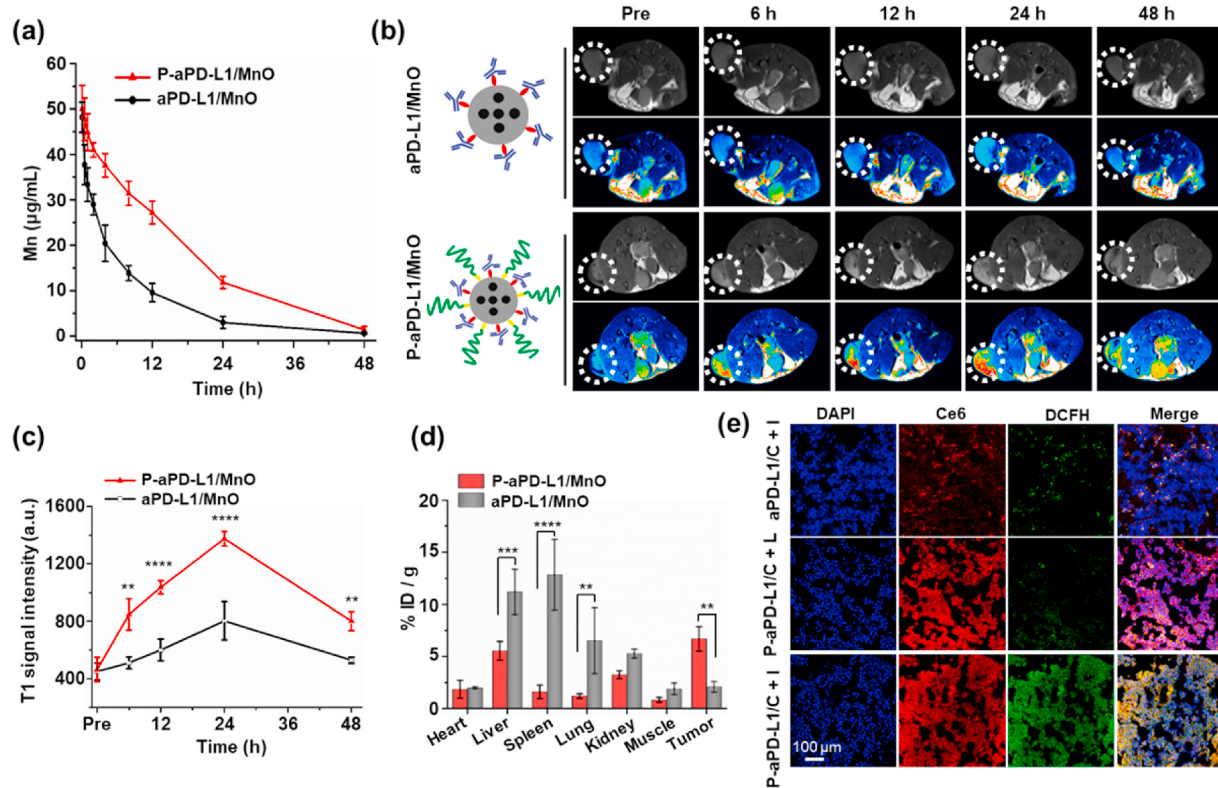


Fig. 4. Pharmacokinetic profiles, tumor accumulation and insonation-induced ROS generation *in vivo*. (a) Pharmacokinetic profiles of P-aPD-L1/MnO and aPD-L1/MnO examined at a Mn dose of 10.0 mg/kg. (b) T1-weighted MR imaging of B16-F10 melanoma before (Pre) and after tail vein injection of P-aPD-L1/MnO or aPD-L1/MnO at different time points. Mn dose was 10 mg/kg body weight. The white dotted portions indicate tumor tissue. (c) Time course quantification of T1-weighted MR signal intensity in tumor. (d) Biodistribution of Mn element measured by ICP-OES at 24 h after intravenous injection of P-aPD-L1/MnO or aPD-L1/MnO. (e) CLSM examination of laser irradiation- or insonation-induced ROS generation in melanoma tissue using DCFH as ROS probe. Insonation (I, 2 MHz, 2.0 W/cm², 20% duty cycle, 10 min) or laser irradiation (L, 670 nm, 200 mW/cm², 10 min, 5 min interval after 5 min) was applied at 24 h after intravenous injection of nanodrug. Data are shown as the mean \pm SD, $n = 3$. * $P < 0.05$, ** $P < 0.01$, and *** $P < 0.001$. Statistical analyses in (c–d) were performed using ANOVA with Tukey's test.

After injecting nanodrug into the B16-F10 melanoma-bearing mice *via* tail vein, the *in vivo* distribution and tumor accumulation of nanodrug was monitored by MRI. As shown in Fig. 4b, both the PEG-coated (P-aPD-L1/MnO) and non-coated (aPD-L1/MnO) nanodrugs accumulated at the tumor sites. Nevertheless, P-aPD-L1/MnO obviously showed a much more efficient tumor accumulation than aPD-L1/MnO at all-time points of measurement up to 48 h. The time point for the highest tumor accumulation was about 24 h after intravenous administration for both P-aPD-L1/MnO and aPD-L1. At this time point, the mice receiving P-aPD-L1/MnO exhibited a 197% increase in the tumor T1-weighted signal intensity, which indicated an approximately 0.7-fold increase as compared to the mice receiving aPD-L1/MnO (Fig. 4c). Additionally, the distributions of P-aPD-L1 and aPD-L1 in major organs and tumor were evaluated *via* measuring the content of Mn element at 24 h after intravenous administration. As shown in Fig. 4d, mice receiving aPD-L1/MnO showed much more Mn than mice receiving P-aPD-L1/MnO in major organs including the liver, spleen and lung, which strongly indicated the on-target but off-tumor effect of aPD-L1/MnO. Moreover, mice receiving P-aPD-L1/MnO showed a higher Mn content in tumor which was approximately 2.2 times higher than mice receiving aPD-L1/MnO ($6.7 \pm 1.2\%$ vs $2.1 \pm 0.5\%$ ID/g), demonstrating again that the PEG-sheddable strategy enhanced the tumor-targeting delivery of the aPD-L1-modified nanodrug. Then, the nanocarrier-mediated tumor accumulation of Ce6 was verified based on the CLSM observation of tumor tissue sections. As shown in Fig. 4e, mice receiving P-aPD-L1/C showed much higher Ce6 fluorescence intensities on the tumor tissue sections than mice receiving aPD-L1/C at 24 h, which was in line with the *in vivo* MR imaging results. Meanwhile, under insonation, mice receiving P-aPD-L1/C showed much stronger DCF fluorescence on the tumor tissue

sections than mice receiving aPD-L1/C, indicating much more effective ROS generation in the P-aPD-L1/C + insonation treatment group. As a comparison, the ROS production of Ce6 in tumor under a 670 nm laser irradiation to trigger PDT was also evaluated [34]. Notably, the laser irradiation resulted in a much lower DCF fluorescence intensity in tumor tissue than the insonation did (Fig. 4e), which clearly indicated that the light-absorbing melanin would limit NIR laser-triggered PDT and highlighted the necessity of using insonation to trigger SDT for effective melanoma treatment.

3.6. Synergistic anticancer effect of immunotherapy and SDT

Animal studies were performed in mice bearing B16-F10 melanoma to evaluate the synergistic anticancer effect of aPD-L1 and SDT *in vivo*. As shown in Fig. 5a and b, all treatments with nanodrugs showed obvious therapeutic effects, and tumor growth was even completely inhibited in mice treated with P-aPD-L1/C + insonation. On day 15 after the first treatment, tumor volume in the P-aPD-L1/C + insonation group was 105 ± 64 mm³. In comparison, tumors grew to 2563 ± 360 mm³, 1499 ± 218 mm³, 1104 ± 129 mm³, and 718 ± 198 mm³ in the PBS control group, P-aPD-L1/C group, P-Iso/C + insonation group, and aPD-L1/C + insonation group, respectively. In line with the tumor growth inhibition results, the P-aPD-L1/C + insonation treatment most effectively prolonged the survival rate of mice, making 83% mice survive longer than 40 days (Fig. 5b). Regardless of different treatments, the body weights of mice in all groups remained stable (Fig. S7). The synergistic immunotherapy and SDT of nanodrug was further explored on tumor tissue sections. As shown in Fig. S8, tumor tissue from animal treated with PBS was hypercellular. In contrast, the cancer cell densities

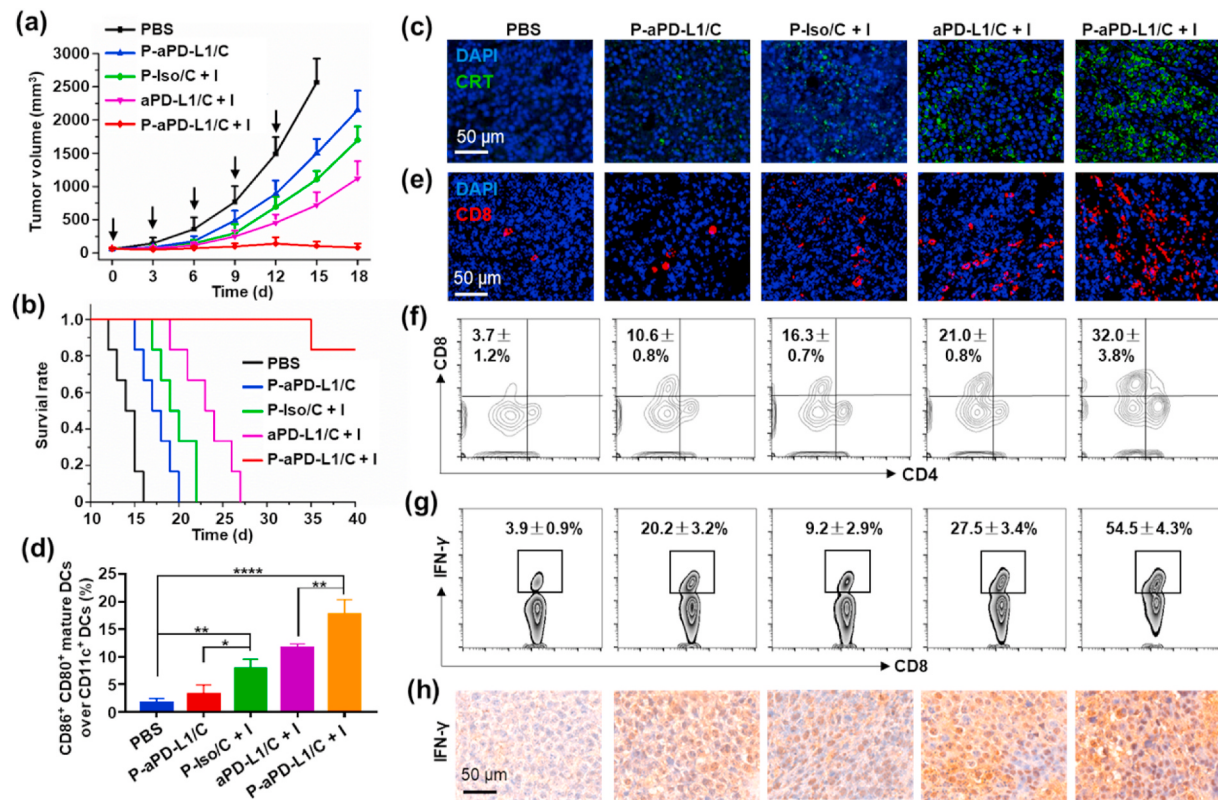


Fig. 5. Synergistic anticancer effects in mice bearing subcutaneous B16-F10 tumor. (a) Tumor growth, and (b) cumulative survivals of animals receiving different treatments via intravenous injections being applied 5 times at an interval of 2 days, as indicated by the black arrows. (c) Immunofluorescent staining of CRT expression of cancer cells induced by different treatments. (d) Proportion of intratumoral mature DCs ($CD86^+ CD80^+$) over $CD11c^+$ DCs measured by flow cytometry. (e) Immunofluorescent staining of intratumoral $CD8^+$ T cells examined by CLSM. (f) Proportion of intratumoral $CD8^+$ T cells over $CD3^+$ T cells measured by flow cytometry. (g) Proportion of intratumoral $CD8$ and $IFN-\gamma$ dual-positive T cells over $CD3^+ CD4^- CD8^+$ T cells measured by flow cytometry. (h) Intratumoral $IFN-\gamma$ expression measured by immunohistochemical staining. Ce6 and antibody were injected 5 times at an interval of 2 days, and their doses were both 5 mg/kg body weight per injection. Insonation (I, 2 MHz, 2.0 W/cm², 20% duty cycle, 10 min) was applied at 24 h after intravenous injection of nanodrug. Tumors were excised and examined on day 15 after the first treatment for (c–h). Data are shown as the mean \pm SD, $n = 6$ for (a–b), and $n = 3$ for (d, f and g). * $P < 0.05$, ** $P < 0.01$, and *** $P < 0.001$. Statistical analyses in (d) were performed using ANOVA with Tukey's test.

in tumor tissues from animals receiving P-aPD-L1/C, P-Iso/C + insonation, or aPD-L1/C + insonation declined obviously. Moreover, tumor tissue from animal treated with P-aPD-L1/C + insonation showed the most significant decrease in cancer cell density. Then, the CRT exposure in tumor was determined to investigate the ICD. Immunofluorescent staining assay revealed that the CRT exposure in tumor tissue was hardly observed in the PBS group (Fig. 5c). In comparison, although the P-aPD-L1/C, P-Iso/C + insonation, and aPD-L1/C + insonation treatments increased the CRT exposure, the P-aPD-L1/C + insonation treatment led to the most remarkable increase in the CRT exposure. The synergistic immunological effect of SDT and aPD-L1 which induced the DCs maturation to express the co-stimulatory molecules CD80/CD86 was verified by flow cytometry analysis [35]. As shown in Fig. 5d and Fig. S9, the P-aPD-L1/C + insonation treatment resulted in a much higher level of DCs maturation (17.7%) than treatments using aPD-L1/C + insonation (11.6%), P-Iso/C + insonation (7.8%), P-aPD-L1/C (3.3%), and PBS (1.7%).

As tumor infiltration of T cells is crucial for immunotherapy [36], the numbers of tumor-infiltrating mature T cells ($CD3^+$) in various treatment groups were measured by flow cytometry. As shown in Fig. S10, without insonation, the effect of P-aPD-L1/C treatment on tumor infiltration of T cells was obviously limited. In comparison, all Ce6-encapsulated nanodrugs including the one carrying an antibody isotype (P-Iso/C) nonspecific to aPD-L1 appeared very effective in promoting the tumor infiltration of T cells when the tumor sites were exposed to ultrasound insonation (2.0 MHz, 2.0 W/cm², 20% duty cycle, 10 min) to induce an additional SDT. Moreover, the mice treated with

P-aPD-L1/C + insonation showed the highest number of tumor-infiltrating $CD3^+$ T cells among all treatment groups. Then, tumor infiltration of the $CD8^+$ T cells was analyzed by immunofluorescent staining of tumor tissue sections (Fig. 5e). In comparison with the rare tumor infiltration of $CD8^+$ T cells in the PBS group, tumor infiltration of $CD8^+$ T cells was obviously increased via treatments of other nanodrugs. In particular, the P-aPD-L1/C + insonation treatment showed the best effect to promote the tumor infiltration of $CD8^+$ T cells. The proportion of tumor-infiltrating T cells ($CD8^+ CD4^-$) over total T cells ($CD3^+$) was further quantified by flow cytometry (Fig. 5f). In comparison with the PBS treatment, the P-aPD-L1/C, P-Iso/C + insonation, and aPD-L1 + insonation treatments increased the proportion of tumor-infiltrating $CD8^+$ T cells. Moreover, the P-aPD-L1/C + insonation treatment was most effective in enhancing the tumor-infiltration of $CD8^+$ T cells, i.e. $32.0 \pm 3.8\%$ for the P-aPD-L1/C + insonation treatment vs $3.7 \pm 1.2\%$ for the PBS treatment. These results showed that the tumor microenvironment (TME)-sensitive nanodrugs may mediate effective aPD-L1 treatment and Ce6-based SDT to enhance the tumor infiltration of $CD8^+$ T cells. More excitingly, a synergistic effect to promote the tumor infiltration of T cells may exist between the aPD-L1 treatment and Ce6-based SDT. The nanodrug with PEG coating (P-aPD-L1/C) appeared more effective than the nanodrug without PEG coating, apparently owing to a better tumor accumulation as already demonstrated (Fig. 4b–d).

In consideration that $IFN-\gamma$ produced by $CD8^+$ T cells can induce the secretion of proinflammatory cytokines for a strong antitumor immunity [37], the intratumoral proportion of $IFN-\gamma^+ CD8^+$ T cells over $CD3^+$

CD4⁻ CD8⁺ T cells was investigated to verify the activation of the tumor-cell killing of T cells. As shown in Fig. 5g, compared with the PBS treatment, single treatment of P-aPD-L1/C or P-Iso/C + insonation induced an increase in the proportion of IFN- γ ⁺ CD8⁺ T cells. Moreover, the proportion of IFN- γ ⁺ CD8⁺ T cells (54.5%) induced by the P-aPD-L1/C + insonation was even much higher than the sum (29.4%) induced by P-aPD-L1/C (20.2%) and P-Iso/C + insonation (9.2%), which implied a strong synergistic effect of aPD-L1 and SDT to initiate anticancer immune response. Due to the high drug delivery efficiency via the PEG sheddable strategy, the proportion of IFN- γ ⁺ CD8⁺ T cells induced by the P-aPD-L1/C + insonation treatment was approximately 1.0-fold higher than that induced by the aPD-L1/C + insonation treatment. The immunohistochemical staining of IFN- γ on tumor sections showed results in line with that of the flow cytometric assay. As shown in Fig. 5h, the P-aPD-L1/C treatment induced the highest IFN- γ secretion, which was attributed to the synergistically enhanced anticancer immune response mediated by a combination of PD-L1 blockade and SDT.

Although the immunocheckpoint antibody therapy, such as aPD-L1 antibody, has shown great potential in the treatment of a variety of tumors, it suffers from immaturity of DCs, insufficient intratumoral infiltration of T cells, and inefficient activation of tumor-specific cytotoxic T lymphocyte (CTL) which result in low immune response rate and poor therapeutic outcome [38–41]. In this study, Ce6-mediated SDT effectively induced the immunogenic cell death (ICD, Fig. 5c) which promoted the maturation of DCs, tumor infiltration of T cells, and activation of CTL (Fig. 5d–h). Consequently, the SDT and tumor-local release of aPD-L1 synergized to evoke a robust anti-cancer immunity which completely inhibited the tumor growth (Fig. 5a).

3.7. Reduction in immune-related adverse effects (irAEs)

Although the certain types of toxicity and side effect of the aPD-L1 and aPD-1 antibodies were smaller than traditional medicine such as chemotherapeutic agents, the immune-related adverse effects (irAEs) were expected and indeed often occurred because the PD-L1/PD-1 signaling pathway modulates the immunologic balance under normal conditions [14,15]. More seriously, patients may die because of the storm of immune cytokines triggered by the treatment of aPD-L1 or aPD-1 antibodies, which remains a great challenge for the clinical applications of ICB-based cancer immunotherapy [42]. For example, there were three drug-related deaths (1%) from pneumonitis in a clinic treatment of NSCLC and CRC using Nivolumab (an anti-PD-1 antibody) [43]. In the present study, the nanodrug was designed to hide aPD-L1 during transportation but expose it inside tumor tissue, which was supposed to reduce the irAEs. The irAEs of nanodrug and free aPD-L1 were evaluated by analyzing liver serum function markers and examining pathological changes of major organs.

As shown in Fig. 6a, the levels of alanine aminotransferase (ALT) and total bilirubin (TBIL) indicating the liver functions were not elevated in mice receiving the treatments of the PEG-sheddable dual-sensitive nanodrugs, P-aPD-L1/C and P-aPD-L1/C + insonation. On the contrary, the ALT and TBIL levels were significantly elevated in mice receiving the treatment of both free aPD-L1 and the nanodrug without PEG coating under insonation (aPD-L1/C + insonation), which indicated the hepatic toxicity due to systematic exposure of aPD-L1. Moreover, tissue injuries in spleen, lung, and liver clearly appeared in mice receiving the treatment of both free aPD-L1 and aPD-L1/C + insonation, whereas the treatments of P-aPD-L1/C and P-aPD-L1 + insonation both showed no obvious tissue damage in these organs (Fig. 6b). Notably, the low

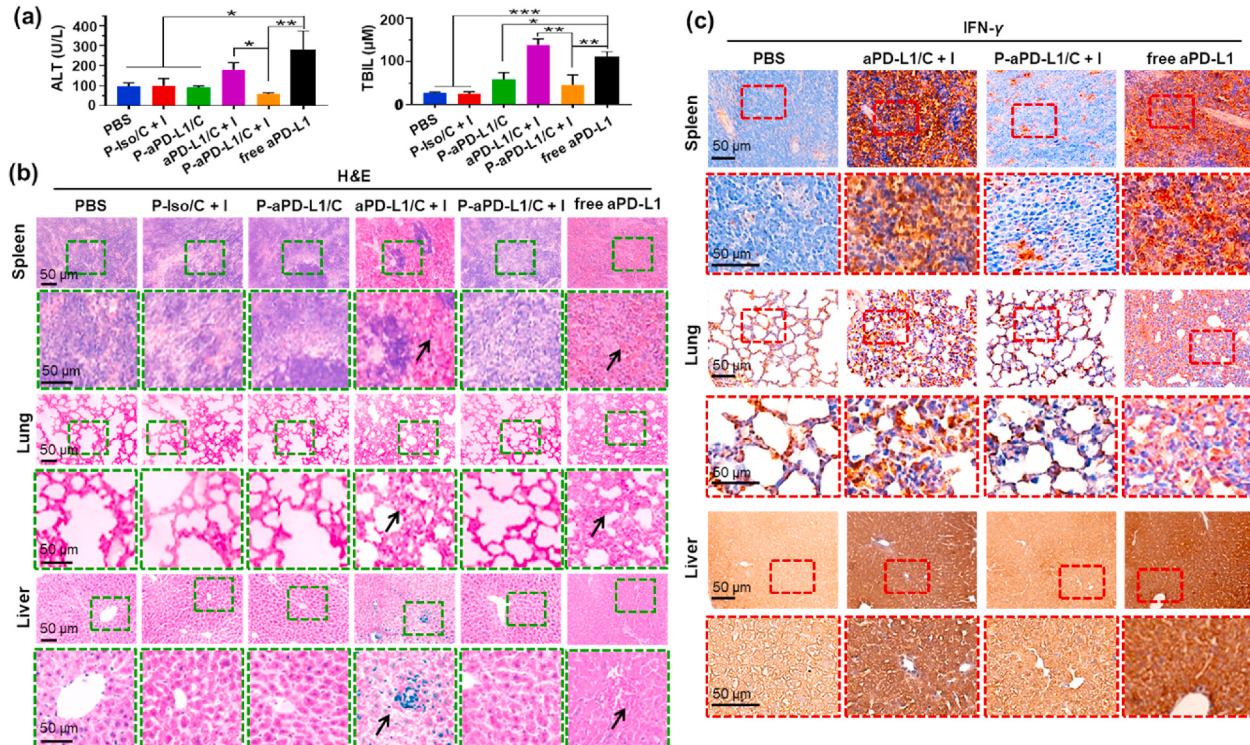


Fig. 6. Side effects in mice bearing subcutaneous B16-F10 tumor on day 15 after the first treatment. (a) Analyses of serum function markers of the liver (ALT and TBIL). (b) *Ex vivo* pathological H&E staining and (c) IFN- γ immunohistochemical staining of the liver, lung, and spleen of mice receiving different treatments. The blood and major organ were collected and examined on day 15 after the first treatment. Nuclei were stained blue, while cytoplasm and extracellular matrix were stained red in H&E staining. Doses of Ce6 and antibody were injected 5 times at an interval of 2 days, and their doses were both 5 mg/kg body weight per injection. The black arrows indicated the tissue injuries or inflammatory. Data are shown as the mean \pm SD in (a), $n = 3$. * $P < 0.05$, ** $P < 0.01$ and *** $P < 0.001$. Statistical analyses in (a) were performed using ANOVA with Tukey's test. (For interpretation of the references to colour in this figure legend, the reader is referred to the Web version of this article.)

intensity ultrasound (2.0 MHz, 2.0 W/cm², 20% duty cycle) was safe and did not cause damage to cells (Fig. S6b). In addition, ultrasound irradiation was focused on the tumor tissue. As shown in Fig. 6a and b, there was no significant difference between the P-aPD-L1/C group and the P-aPD-L1/C + I group for the side effects in spleen, lung, and liver, indicating the focal ultrasound irradiation did not induce a toxic effect on spleen, lung, and liver. Therefore, the side effects of spleen and liver in aPD-L1/C + I group were not came from the ultrasound irradiation.

The immunohistochemical staining of IFN- γ on the sections of liver, lung, and spleen from mice receiving different treatments was analyzed to study the immune cytokine storm induced by systemic immunity. IFN- γ is mainly secreted by activated T lymphocytes (especially CD8⁺ T cells) and NK cells, and has a strong effect on promoting immune and inflammatory response [44–46]. As shown in Fig. 6c, compared with the PBS group, IFN- γ expression in spleen, lung and liver tissues was significantly elevated in the both free aPD-L1 and aPD-L1/C + I groups. However, no significant increase in IFN- γ expression was observed in the P-aPD-L1/C + I group. The above data demonstrated that irAEs were induced by systematic exposure of aPD-L1, and the tumor-targeting

delivery of aPD-L1 with the PEG-sheddable dual-sensitive nanocarrier not only efficiently induced the tumor-local immunotherapy but also significantly alleviated the irAEs.

3.8. Immune memory effects in vivo

The immune memory effect is crucial for durable tumor inhibition and recurrence prevention [47]. As illustrated in Fig. 7a, the tumor recurrence was overseen and the tumor rechallenge test was performed to reveal the nanodrug-elicited antitumor immune memory effect in mice bearing primary B16-F10 tumor. As shown in Fig. 7b, the tumor recurrence occurred in all mice receiving PBS. In addition, the tumor recurrence was found in most mice receiving P-aPD-L1/C, P-Iso/C + insonation, and aPD-L1/C + insonation. Excitingly, tumor recurrence was not detected in mice receiving P-aPD-L1/C + insonation. Next, the mice receiving different treatments were rechallenged with the secondary homotypic tumor after the surgical resection of primary tumor. As shown in Fig. 7c, the treatments of P-aPD-L1/C, P-Iso/C + insonation, and aPD-L1/C showed negligible benefits in the inhibition of secondary

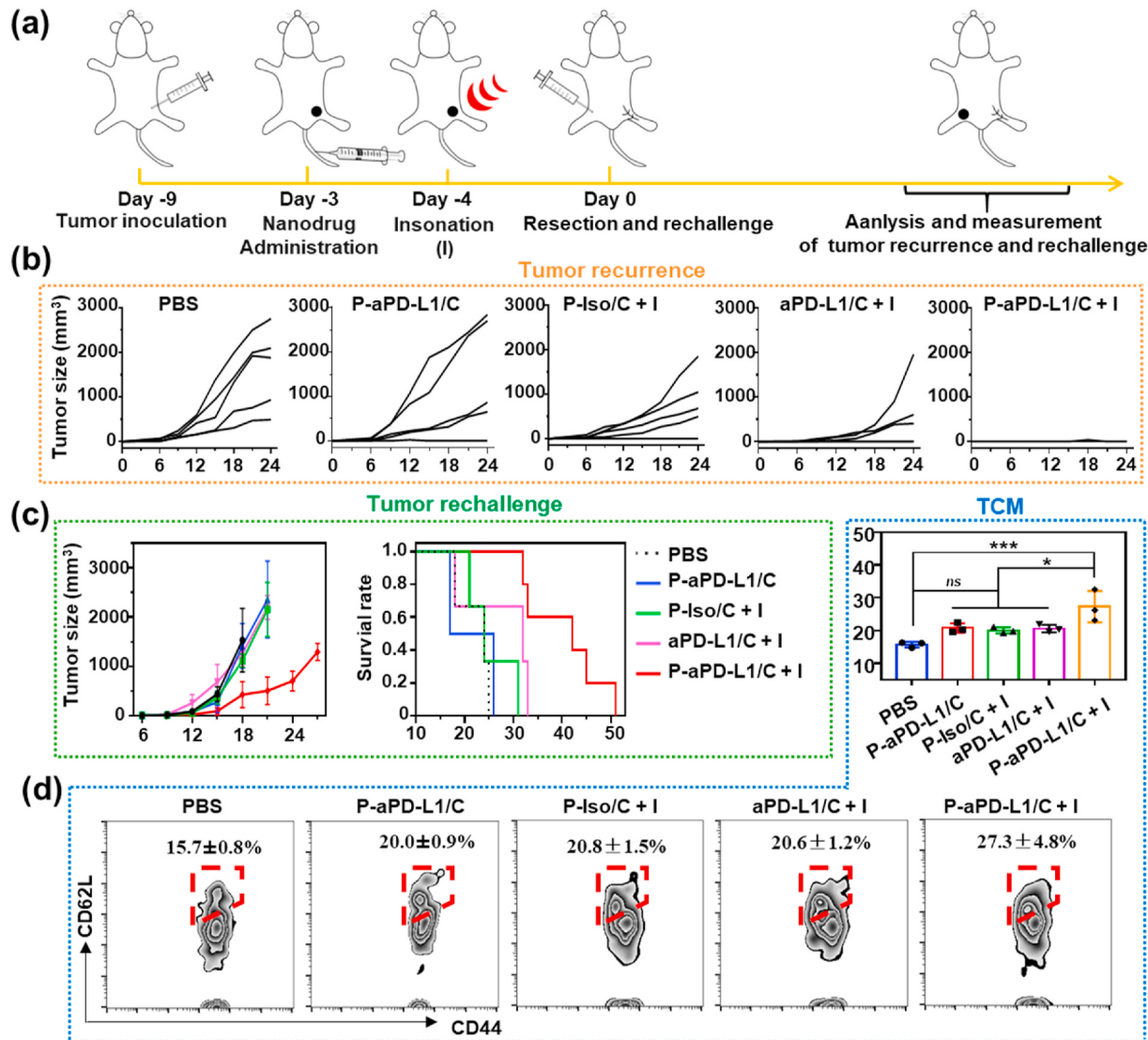


Fig. 7. Synergistic anti-tumor immune memory effect of P-aPD-L1/C. (a) Schematic illustration of the studies of B16-F10 tumor recurrence and rechallenge. (b) Individual tumor growth curves of tumor recurrence in mice receiving different treatments. (c) Secondary B16-F10 tumor growth and cumulative survivals of animals receiving tumor rechallenge. (d) Proportion of central memory T cells (TCM, CD62L⁺ CD44⁺) over CD3⁺ CD8⁺ T cells in blood on day 14 after the first treatment measured by flow cytometry. Data are shown as the mean \pm SD, $n = 5$ for (c), and $n = 3$ for (d). * $P < 0.05$, ** $P < 0.01$, *** $P < 0.001$, and ns represents no significant difference. Statistical analyses in (d) were performed using ANOVA with Tukey's test.

tumor as compared with the PBS group. However, the secondary tumor growth was effectively inhibited in mice receiving P-aPD-L1/C + insonation. Consistently, the best survival benefit was also observed with the P-aPD-L1/C + insonation treatment. That is, 50% of mice survived long than 41 d, which suggested that the P-aPD-L1/C + insonation treatment elicited durable immune responses against the secondary tumor. Admittedly, the central memory T cells (TCM) have a long survival time *in vivo*, and could proliferate and differentiate into effective memory T cells after tumor antigen stimulation, thus playing a key role in long-term anti-tumor [48]. Therefore, the proportion of TCM (CD3⁺ CD8⁺ CD62L⁺ CD44⁺) was measured to explore the immune memory effect. As shown in Fig. 7d, in comparison with the treatment of PBS, the treatments of P-aPD-L1/C, P-Iso/C + insonation, and aPD-L1/C + insonation showed negligible increase in the proportion of TCM. In contrast, the P-aPD-L1/C + insonation treatment resulted in a significant increase in the proportion of TCM, indicating a strong immune memory response elicited by a synergistic SDT and aPD-L1 therapy using the PEG-coated dual-sensitive nanodrug.

4. Conclusions

A PEG coating-sheddable micellar nanodrug encapsulating a sonosensitizer (Ce6) in its core and conjugating aPD-L1 to its interlayer through MMP-2-cleavable peptide was prepared based on biosafe lipids for the immuno-sonodynamic antitumor therapy. The PEG coating was sable at pH 7.4 but detached inside tumor tissue (pH 6.5) to enable a pH-triggered stealth-to-nonstealth conversion, which not only activated the local anti-tumor immunity and but also reduced systemic irAEs. The PEG detachment and MMP-2-triggered aPD-L1 release inside tumor turned the negatively charged nanodrug into a positively charged one, thereby facilitating the Ce6 delivery into cancer cells. In addition to the tumor-specific immune checkpoint blockade with aPD-L1, SDT implemented under low intensity insonation produced ROS to kill the cancer cells, thereby releasing tumor-associated antigens. As a result, the aPD-L1 treatment and SDT synergistically promoted the activation and tumor infiltration of cytotoxic T cells to elicit robust anti-cancer immunity and long-term immune memory which effectively suppressed melanoma growth and postoperative recurrence. As far as we know, the tumor-targeting codelivery of immune checkpoint inhibitor and sonosensitizer based on biosafe lipids carrier for immuno-sonodynamic anti-melanoma therapy has not been reported yet. This strategy reduced systemic irAEs and bypassed the poor light penetration, which showed great promise for the synergistic immuno-sonodynamic treatment of pigmented and deeply seated tumor.

Credit author statement

Jinsheng Huang, Methodology, Writing – original draft, Investigation, and Funding acquisition. Zecong Xiao, Methodology, Investigation, and Formal analysis. Yongcheng An, Investigation. Shisong Han, Investigation, and Funding acquisition. Wei Wu, Investigation, and Validation. Yong Wang, Data curation, Validation, and Funding acquisition. Yu Guo, Visualization, Project administration, and Funding acquisition. Xintao Shuai, Supervision, Writing – review & editing, Conceptualization, and Funding acquisition.

Data availability

The data used in the present study are available from the corresponding author on reasonable request.

Author contribution

J. Huang and Z. Xiao contributed equally to this work. X. Shuai., Y. Wang, and Y. Guo conceived and designed the nanodrug and experimental program. J. Huang., Z. Xiao., Y. An., S. Han., W. Wu., Y. Wang,

and Y. Guo. performed the experiments and data analysis. X. Shuai., J. Huang., and Z. Xiao. wrote the manuscript. All authors contributed feedback on the final manuscript.

Declaration of competing interest

The authors declare that they have no known competing financial interests or personal relationships that could have appeared to influence the work reported in this paper.

Acknowledgements

This research was supported by the National Natural Science Foundation of China (51933011, 31971296, 21905112, 21805314, 51703257), the Key Areas Research and Development Program of Guangzhou (202007020006), the Key Areas Research and Development Program of Guangdong (2019B020235001), and the China Postdoctoral Science Foundation (2019M663380).

Appendix B. Supplementary data

Supplementary data to this article can be found online at <https://doi.org/10.1016/j.biomaterials.2020.120636>.

Appendix A. Supplementary data

Supplementary material related to this article can be found, in the online version.

References

- [1] D. Schadendorf, A.C.J. van Akkooi, C. Berking, K.G. Griewank, R. Gutzmer, A. Hauschild, A. Stang, A. Roesch, S. Ugurel, Melanoma, *The Lancet* 392 (2018) 971–984, 10151.
- [2] B. Domingues, J.M. Lopes, P. Soares, H. Pópolo, Melanoma treatment in review, *ImmunoTargets Ther.* 7 (2018) 35–49.
- [3] J. Xu, L. Xu, C. Wang, R. Yang, Q. Zhuang, X. Han, Z. Dong, W. Zhu, R. Peng, Z. Liu, Near-infrared-triggered photodynamic therapy with multitasking upconversion nanoparticles in combination with checkpoint blockade for immunotherapy of colorectal cancer, *ACS Nano* 11 (5) (2017) 4463–4474.
- [4] M. Wainwright, Therapeutic applications of near-infrared dyes, *Color. Technol.* 126 (3) (2010) 115–126.
- [5] C. McEwan, H. Nesbitt, D. Nicholas, O.N. Kavanagh, K. McKenna, P. Loan, I. G. Jack, A.P. McHale, J.F. Callan, Comparing the efficacy of photodynamic and sonodynamic therapy in non-melanoma and melanoma skin cancer, *Biorg. Med. Chem.* 24 (13) (2016) 3023–3028.
- [6] P. Huang, X. Qian, Y. Chen, L. Yu, H. Lin, L. Wane, Y. Zhu, J. Shi, Metalloporphyrin-encapsulated biodegradable nanosystems for highly efficient magnetic resonance imaging-guided sonodynamic cancer therapy, *J. Am. Chem. Soc.* 139 (3) (2017) 1275–1284.
- [7] J. Ouyang, Z. Tang, N. Farokhzad, N. Kong, N.Y. Kim, C. Feng, S. Blake, Y. Xiao, C. Liu, T. Xie, W. Tao, Ultrasound mediated therapy: recent progress and challenges in nanoscience, *Nano Today* 35 (2020) 100949.
- [8] N. Nomikou, C. Fowlley, N.M. Byrne, B. McCaughey, A.P. McHale, J.F. Callan, Microbubble-sonosensitiser conjugates as therapeutics in sonodynamic therapy, *Chem. Commun.* 48 (67) (2012) 8332–8334.
- [9] Y. Chen, H. Chen, Y. Sun, Y. Zheng, D. Zeng, F. Li, S. Zhang, X. Wang, K. Zhang, M. Ma, Q. He, L. Zhang, J. Shi, Multifunctional mesoporous composite nanocapsules for highly efficient MRI-guided high-intensity focused ultrasound cancer Surgery, *Angew. Chem. Int. Ed.* 50 (52) (2011) 12505–12509.
- [10] W. Yue, L. Chen, L. Yu, B. Zhou, H. Yin, W. Ren, C. Liu, L. Guo, Y. Zhang, L. Sun, K. Zhang, H. Xu, Y. Chen, Checkpoint blockade and nanosonosensitizer-augmented noninvasive sonodynamic therapy combination reduces tumour growth and metastases in mice, *Nat. Commun.* 10 (2019) 2025.
- [11] D. Hanahan, R.A. Weinberg, Hallmarks of cancer: the next generation, *Cell* 144 (5) (2011) 646–674.
- [12] A. Ribas, J.D. Wolchok, Cancer immunotherapy using checkpoint blockade, *Science* 359 (6382) (2018) 1350–1355.
- [13] M. Mansh, Ipilimumab and cancer immunotherapy: a new hope for advanced stage melanoma, *Yale J. Biol. Med.* 84 (4) (2011) 381–389.
- [14] R. Deng, D. Bumbaca, C.V. Pastuskovas, C.A. Boswell, D. West, K.J. Cowan, H. Chiu, J. McBride, C. Johnson, Y. Xin, H. Koeppen, M. Leabman, S. Iyer, Preclinical pharmacokinetics, pharmacodynamics, tissue distribution, and tumor penetration of anti-PD-L1 monoclonal antibody, an immune checkpoint inhibitor, *mAbs* 8 (3) (2016) 593–603.
- [15] Y. Wang, D.H. Wiesnoski, B.A. Helmink, V. Gopalakrishnan, K. Choi, H.L. DuPont, Z.-D. Jiang, H. Abu-Sbeih, C.A. Sanchez, C.-C. Chang, E.R. Parra, A. Francisco-Cruz,

- G.S. Raju, J.R. Stroehlein, M.T. Campbell, J. Gao, S.K. Subudhi, D.M. Maru, J. M. Blando, J.P. Allison, P. Sharma, M.T. Tetzlaff, J.A. Wargo, R.R. Jenq, Fecal microbiota transplantation for refractory immune checkpoint inhibitor-associated colitis, *Nat. Med.* 24 (12) (2018) 1804–1808.
- [16] L. Milling, Y. Zhang, D.J. Irvine, Delivering safer immunotherapies for cancer, *Adv. Drug Deliv. Rev.* 114 (2017) 79–101.
- [17] J. Park, S.H. Wrzesinski, E. Stern, M. Look, J. Criscione, R. Ragheb, S.M. Jay, S. L. Demento, A. Agawu, P. Licona Limon, A.F. Ferrandino, D. Gonzalez, A. Habermann, R.A. Flavell, T.M. Fahmy, Combination delivery of TGF- β inhibitor and IL-2 by nanoscale liposomal polymeric gels enhances tumour immunotherapy, *Nat. Mater.* 11 (10) (2012) 895–905.
- [18] J. Huang, Y. Xu, H. Xiao, Z. Xiao, Y. Guo, D. Cheng, X. Shuai, Core-shell distinct nanodrug showing on-demand sequential drug release to act on multiple cell types for synergistic anticancer therapy, *ACS Nano* 13 (6) (2019) 7036–7049.
- [19] C.-Y. Sun, Y. Liu, J.-Z. Du, Z.-T. Cao, C.-F. Xu, J. Wang, Facile generation of tumor-pH-labile linkage-bridged block copolymers for chemotherapeutic delivery, *Angew. Chem. Int. Ed.* 55 (3) (2016) 1010–1014.
- [20] H.B. Na, J.H. Lee, K.J. An, Y.I. Park, M. Park, I.S. Lee, D.H. Nam, S.T. Kim, S. H. Kim, S.W. Kim, K.H. Lim, K.S. Kim, S.O. Kim, T. Hyeon, Development of a T-1 contrast agent for magnetic resonance imaging using MnO nanoparticles, *Angew. Chem. Int. Ed.* 46 (28) (2007) 5397–5401.
- [21] L.T. Lin, H.Y. Gong, R. Li, J.J. Huang, M.Y. Cai, T. Lan, W.S. Huang, Y.J. Guo, Z. M. Zhou, Y.C. An, Z.W. Chen, L.C. Liang, Y. Wang, X.T. Shuai, K.S. Zhu, Nanodrug with ROS and pH dual-sensitivity ameliorates liver fibrosis via multicellular regulation, *Adv. Sci.* 7 (7) (2020) 15.
- [22] M. Mühlbauer, M. Fleck, C. Schütz, T. Weiss, M. Froh, C. Blank, J. Schölmerich, C. Hellerbrand, PD-L1 is induced in hepatocytes by viral infection and by interferon- α and - γ and mediates T cell apoptosis, *J. Hepatol.* 45 (4) (2006) 520–528.
- [23] S. Kim, M. Fujitsuka, T. Majima, Photochemistry of singlet oxygen sensor green, *J. Phys. Chem. B* 117 (45) (2013) 13985–13992.
- [24] M. Yu, X. Xu, Y. Cai, L. Zou, X. Shuai, Perfluorohexane-cored nanodroplets for stimulations-responsive ultrasonography and O2-potentiated photodynamic therapy, *Biomaterials* 175 (2018) 61–71.
- [25] Y. Jiang, J. Li, X. Zhen, C. Xie, K. Pu, Dual-peak absorbing semiconducting copolymer nanoparticles for first and second near-infrared window photothermal therapy: a comparative study, *Adv. Mater.* 30 (14) (2018).
- [26] C. Bremer, C.-H. Tung, R. Weissleder, In vivo molecular target assessment of matrix metalloproteinase inhibition, *Nat. Med.* 7 (6) (2001) 743–748.
- [27] Z. Su, Z. Xiao, Y. Wang, J. Huang, Y. An, X. Wang, X. Shuai, Codelivery of anti-PD-1 antibody and paclitaxel with matrix metalloproteinase and pH dual-sensitive micelles for enhanced tumor chemoimmunotherapy, *Small* 16 (7) (2020) 1906832.
- [28] R.P. Singh, H.V. Gangadharappa, K. Mruthunjaya, Phospholipids: unique carriers for drug delivery systems, *J. Drug Deliv. Sci. Technol.* 39 (2017) 166–179.
- [29] V. Postupalenko, D. Desplancq, I. Orlov, Y. Arntz, D. Spehner, Y. Mely, B. P. Klaholz, P. Schultz, E. Weiss, G. Zuber, Protein delivery system containing a nickel-immobilized polymer for multimerization of affinity-purified his-tagged proteins enhances cytosolic transfer, *Angew. Chem. Int. Ed.* 54 (36) (2015) 10583–10586.
- [30] C.R. Zobel, J.Y. Roe, Positive staining of protein molecules for electron microscopy, *Biochim. Biophys. Acta* 133 (1) (1967) 157–161.
- [31] Y. Lu, A.A. Aimetti, R. Langer, Z. Gu, Bioresponsive materials, *Nat. Rev. Mater.* 2 (1) (2017) 16075.
- [32] G. Kroemer, L. Galluzzi, O. Kepp, L. Zitvogel, Immunogenic cell death in cancer therapy, *Annu. Rev. Immunol.* 31 (2013) 51–72.
- [33] H. Xiao, X. Li, C. Zheng, Q. Liu, C. Sun, J. Huang, Y. Wang, Y. Yuan, Intracellular pH-sensitive polymeric micelle for simultaneous chemotherapy and MR imaging of hepatocellular carcinoma, *J. Nano Res.* 22 (5) (2020) 105.
- [34] X. Li, S. Lee, J. Yoon, Supramolecular photosensitizers rejuvenate photodynamic therapy, *Chem. Soc. Rev.* 47 (4) (2018) 1174–1188.
- [35] G. De la Rosa, D. Yang, P. Tewary, A. Varadhachary, J.J. Oppenheim, Lactoferrin acts as an alarmin to promote the recruitment and activation of APCs and antigen-specific immune responses, *J. Immunol.* 180 (10) (2008) 6868–6876.
- [36] I. Melero, A. Rouzaut, G.T. Motz, G. Coukos, T-cell and NK-cell infiltration into solid tumors: a key limiting factor for efficacious cancer immunotherapy, *Cancer Discov.* 4 (5) (2014) 522–526.
- [37] V. Berner, H. Liu, Q. Zhou, K.L. Alderson, K. Sun, J.M. Weiss, T.C. Back, D.L. Longo, B.R. Blazar, R.H. Wiltrout, L.A. Welniak, D. Redelman, W.J. Murphy, IFN- γ mediates CD4+ T-cell loss and impairs secondary antitumor responses after successful initial immunotherapy, *Nat. Med.* 13 (3) (2007) 354–360.
- [38] J. Hsu, J.J. Hodgins, M. Marathe, C.J. Nicolai, M.C. Bourgeois-Daigneault, T. N. Trevino, C.S. Azimi, A.K. Scheer, H.E. Randolph, T.W. Thompson, L. Zhang, A. Iannello, N. Mathur, K.E. Jardine, G.A. Kirn, J.C. Bell, M.W. McBurney, D. H. Raulet, M. Ardolino, Contribution of NK cells to immunotherapy mediated by PD-1/PD-L1 blockade, *J. Clin. Invest.* 128 (10) (2018) 4654–4668.
- [39] Z. Li, Y. Wang, Y. Shen, C. Qian, D. Oupicky, M. Sun, Targeting pulmonary tumor microenvironment with CXCR4-inhibiting nanocomplex to enhance anti-PD-L1 immunotherapy, *Sci. Adv.* 6 (20) (2020).
- [40] P. Sharma, J.P. Allison, The future of immune checkpoint therapy, *Science* 348 (6230) (2015) 56–61.
- [41] M. Versteven, J.M.J. Van den Bergh, E. Marcq, E.L.J. Smits, V.F.I. Van Tendeloo, W. Hobo, E. Lion, Dendritic cells and programmed death-1 blockade: a joint venture to combat cancer, *Front. Immunol.* 9 (2018) 13.
- [42] M.A. Postow, R. Sidlow, M.D. Hellmann, Immune-related adverse events associated with immune checkpoint blockade, *N. Engl. J. Med.* 378 (2) (2018) 158–168.
- [43] K. Ratermann, J. Cox, L. Benitez, F. Davis, Drugs that act on the immune system: cytokines and monoclonal antibodies, side eff., *Drugs Annu* 40 (2018) 477–487.
- [44] J.R. Schoenborn, C.B. Wilson, Regulation of interferon-gamma during innate and adaptive immune responses, *Adv. Immunol.* 96 (2007) 41–101.
- [45] P.S. de Araújo-Souza, S.C. Hanschke, J.P. Viola, Epigenetic control of interferon-gamma expression in CD8 T cells, *J. Immunol. Res.* 2015 (2015) 849573.
- [46] S.J. Szabo, B.M. Sullivan, S.L. Peng, L.H. Glimcher, Molecular mechanisms regulating Th1 immune responses, *Annu. Rev. Immunol.* 21 (2003) 713–758.
- [47] L. Zitvogel, L. Apetoh, F. Ghiringhelli, G. Kroemer, Immunological aspects of cancer chemotherapy, *Nat. Rev. Immunol.* 8 (1) (2008) 59–73.
- [48] C.A. Klebanoff, L. Gattinoni, N.P. Restifo, Sorting through subsets: which T-cell populations mediate highly effective adoptive immunotherapy? *J. Immunother.* 35 (9) (2012) 651–660.